

Evolution of distributions and spatial correlations of single-particle forces and stresses during compression of ductile granular materials

Göran Frenning and Göran Alderborn

Department of Pharmacy, Uppsala University, P. O. Box 580, SE-751 23, Uppsala, Sweden

(Received 9 July 2004; revised manuscript received 6 October 2004; published 25 January 2005)

Uniaxial compression of disordered packings of millimeter-sized ductile particles formed from microcrystalline cellulose is investigated experimentally, at compression pressures in the vicinity of the minimum pressure required to form a coherent compact. Distributions of normal forces and stresses exerted by individual particles on a confining wall are determined. Spatial force and stress correlations are investigated. The distribution of normal forces is found to narrow with increasing pressure, but no indication of a crossover to a Gaussian decay at high forces is observed. The distribution of normal stresses is found to be considerably more Gaussian in shape for all pressures investigated. This finding may be interpreted as resulting from a positive correlation between the area corresponding to each particle and the force it experienced during compression. Spatial force and stress correlations are observed for distances smaller than three particle diameters. The spatial stress correlations indicate that the mode of stress transmission changes when the compression pressure exceeds the minimum pressure required to form a coherent compact.

DOI: 10.1103/PhysRevE.71.011305

PACS number(s): 81.05.Rm, 83.80.Fg, 45.70.Cc, 05.40.-a

I. INTRODUCTION

Granular materials are comprised of collections of individual particles which, as a result of their relatively large size (1 μm or larger), are virtually unaffected by thermal agitation [1,2]. Particulate matter of this kind is important in many areas of physics and engineering science, ranging from astronomy and space physics to geoscience and pharmaceutical technology. Granular matter behaves differently from other familiar forms of matter (solids, liquids, and gases), exhibiting fascinating static and dynamic behaviors, and should therefore be considered as an additional state of matter in its own right [1].

Force is transmitted between the particles of a granular material via the interparticle contacts. As a result of the stochastic nature of these contacts, certain load-bearing structures—force chains—are formed within granular materials, either when loaded or under their own weight. Such force chains may be visualized using stress-induced birefringence [3]. The existence of force chains within granular matter is reflected by a rather wide distribution for the interparticle contact forces. This force distribution is usually probed by investigation of the normal forces exerted by individual particles on a confining surface in uniaxial compression. Whereas the force distribution thus obtained is the only force distribution that is immediately accessible experimentally, it may in some cases be different from the distribution of interparticle contact forces in the bulk of the material [4,5] (see below). Experiments [3,6–10] and simulations [11–17] have revealed that the force distribution generally has two intriguing features: There is an abundance of forces much smaller than the average force $\langle F \rangle$, and the force distribution has an exponential decay for forces $F > \langle F \rangle$. The large proportion of small forces is usually interpreted as an effect of arching [18,19] or jamming [20,21]. In simulations, a power-law behavior has often been observed in this region [11,13,15]. Around $\langle F \rangle$ a plateau or a peak is usually observed in the

force distribution; the appearance of a peak has been argued to be the signature of jamming [22]. The exponential decay has been captured by the scalar q model of force transmission through bead packs [3,23], by the α model [24], and also by a hyperbolic tensorial model, originally developed to account for the stress distribution in sand piles [25–27], but only in the limit of large disorder [28]. An exponential decay was also predicted by the model put forward by Edwards and Grinev [29].

Whereas the force distribution has been found to be largely insensitive to changes in particle arrangement or interparticle friction [8], there is some, albeit somewhat conflicting, evidence suggesting a dependence on the degree of particle deformation [4,9,30–33]. At $\approx 2\%$ deformation [9], a transition to a Gaussian behavior has been observed in two-dimensional (2D) shear experiments [30]. Makse *et al.* have presented some experimental evidence for a transition from an exponential to a Gaussian decay already at $\approx 0.4\%$ deformation [31], but their results conflict with other observations [7,8]. Erikson *et al.* have used a layer of glass beads in between packings of deformable beads and the bottom surface in order to determine the distribution of normal forces [9]. They found that the peak at the mean force increased in height and that the exponential decay became steeper with increasing deformation, but no crossover to a Gaussian behavior was observed. Simulations of granular media sheared under a constant mean stress condition have revealed that the behavior of the force distribution for forces smaller than average depends strongly on shearing, but that the exponential decay at large forces remains [33]. A generalization of the scalar q model that interpolates between granular and elastic regimes has, on the other hand, indicated that deformation should have a decisive influence on the force distribution [32].

The distinction between the experimentally accessible wall-force distribution and the distribution of bulk contact forces may shed additional light on the subject. Recent simu-

lations on 2D packings of Herzian spheres have indicated that changes in the wall-force distribution are dominated by changes in the contact network, while the bulk-force distribution remains remarkably robust [4,5]. Even though the bulk-force distribution remains unaltered, the contact geometry and, in particular, the number of downward-pointing contact forces may change, producing the effects seen in some experiments. Indeed, the experimental findings of Ref. [9] have been reinterpreted along these lines [5].

Another intriguing question is the existence of spatial force correlations, and their evolution with increasing particle deformation. Two-dimensional shear experiments have indicated that correlation effects not present in the q model are important [34]. As long as the q values of different sites are uncorrelated, there are no lateral two-point force correlations at infinite depth in the q model, irrespective of the distribution used [35], but the relaxation toward this limit may be slow [36]. From the analysis of an extension of the q model it has been concluded that the slope of the exponential decay for larger than average forces and the exponent of the power-law valid for small forces both are strongly dependent on the average force-chain length, which should be affected by spatial force correlations [37]. Conflicting results for spatial force correlations between model and simulation were observed in Ref. [32]. Spatial force correlations have been observed in simulations [16] and some experiments [7] but not in others [6].

In this article we use the carbon paper technique [3,6,8,9] to investigate uniaxial compression of packings of millimeter-sized more or less spherical particles formed from microcrystalline cellulose. Such particles are often referred to as pellets. Particles of this type are known to deform plastically, and to form coherent compacts at large pressures, a fact that is much used in pharmaceutical technology [38]. This type of behavior is particularly interesting, since it represents a transition from a fragile material [20], unable to withstand tensile forces, to a coherent body, which usually is well described by continuum models. Measurements are performed in the regimes of both fragile packings and coherent compacts.

For microcrystalline cellulose particles, interparticle bonding is generally believed to be dominated by intermolecular forces (such as hydrogen and van der Waals forces) acting between surfaces brought into close proximity to each other by the compression process [39]. The static (dynamic) coefficient of friction between sheets composed of dry cellulose fibers has been determined as approximately 0.45 (0.3) [40], indicating that the interparticle contacts are frictional.

We, moreover, use the watershed algorithm [41,42] to nonambiguously subdivide each image of imprints into a number of exclusive subregions, each of which corresponds to the imprint made by a single particle. This subdivision is made in such a way that the union of all subregions covers the image (the watershed algorithm hence generates a tessellation of the image area). In this way we are able to determine not only the normal force but also the corresponding normal stress exerted by the particle.

Note that the stress thus defined refers to single particles and hence is distinct from the macroscopic stress field that is obtained by coarse-graining over many particles. The experi-

mental results indicate that the single-particle stress statistics is a better indicator for the transition to a continuum than the force statistics.

Finally, spatial force and stress correlations are investigated.

II. MATERIALS AND METHODS

A. Materials

Particles (pellets) were formed from microcrystalline cellulose (MCC; Avicel PH101, FMC, Ireland, apparent density of 1.571 g/cm^3). Distilled water was used as granulation liquid. Black carbon paper (Radex 1200, Kores, Austria) and white photo-quality paper (Epson Photo Quality Ink Jet Paper, Seiko Epson Corp., Japan) were used for the force measurements.

B. Preparation of particles

The particles investigated in this study were made by wet granulation followed by extrusion and spheronization. The MCC powder (360 g) was agitated in a planetary mixer (QMM-II, Donsmark Process Technology, Denmark) at 500 rpm for 5 min and the granulation liquid (400 g) was then sprayed (Schlick, Model 940, Germany) into the mass at a rate of $\approx 100 \text{ ml/min}$. Wet mixing was continued for 5 min at 500 rpm. The wet powder mass was immediately extruded (model E140, NICA System, Sweden; holes 1.0 mm in diameter and 1.2 mm long) and spheronized (model S 320-450, NICA System) for 3 min on a 32 cm diameter friction plate with radially designed grid at a rotation speed of 800 rpm. The particles were spread out on plates in a thin layer and dried under ambient conditions for 4 days. The size fraction 800–900 μm was separated by dry sieving using a set of standard sieves with square openings (Endecotts, United Kingdom), mechanically shaken (Retsch, Type RV, Germany) for 10 min at a relative agitation intensity of 30. This size fraction was used exclusively in the remainder of the experiments. The particles were stored in a desiccator (over a saturated K_2CO_3 solution) at 40% relative humidity and room temperature for at least 1 month before further investigation. Previous experience shows that particles prepared in this manner have a porosity of $\approx 10\%$ [43].

C. Characterization of particle size and shape

Approximately 800 particles were spread out on a flatbed scanner (Epson Perfection 1640SU Scanner, Seiko Epson Corp., Japan) and covered by a piece of black paper. A digital image with a resolution of 1600 dpi was acquired. The image was analyzed by the noncommercial image-analysis software IMAGEJ (see Sec. II F below). The projected-area diameter $d_p = 2\sqrt{A_p/\pi}$, where A_p is the projected area of the particle, was used as a measure of the particle size. The aspect ratio was used as a measure of the particle roundness (because of the limited resolution of the image, it was not possible to determine the circularity, since the perimeter values obtained were inaccurate).

D. Compression of single particles

Uniaxial compression experiments were performed on single particles by using a Zwick Z100 materials tester (Zwick/Roell, Zwick GmbH & Co. KG, Germany) equipped with a 1 kN load cell. A stationary lower punch (diameter 11.3 mm) was mounted on the lower grip. Pieces of white paper and carbon paper were placed on the lower punch, and a particle was placed on top. The upper punch was lowered at a rate of 1 mm/min until the desired force was reached, and then immediately raised. Forces between 1 and 200 N were used. For each force, five replications were made.

E. Compression of particle packings

Uniaxial compression experiments were performed on particle packings by using the same materials tester now equipped with a 100 kN load cell. A stationary lower punch (diameter 11.3 mm) and a matrix were mounted on the lower grip, and a mobile upper punch on the load cell. Circular pieces (diameter 11 mm) of white paper and carbon paper were placed on the lower punch, 1 g of particles was poured into the die (corresponding to a filling height of approximately 13 mm), and pieces of carbon paper and white paper were placed on top. The upper punch was lowered at a rate of 10 mm/min, until the desired pressure was reached, and then immediately raised at the same rate. Six different compression pressures between 10 and 50 MPa were used, and for each pressure 20 replications were made. Following compression, the particle packing (or the compact) was immediately ejected from the matrix. When a coherent compact was formed, its strength was assessed by diametrical compression at a rate of 1 mm/min within ≈ 1 min after compression by using a tablet-testing instrument (Holland C50, United Kingdom). The imprints made by the particles on the pieces of white paper were converted to electronic form by using the Epson scanner and a resolution of 1600 dpi.

F. Image analysis

The background-corrected digital images of the imprints were analyzed by using the noncommercial software IMAGEJ [51]. The IMAGEJ implementation (written by Sage) of the watershed algorithm originally developed by Vincent and Soille [41] was used to nonambiguously subdivide the region of interest of each image into a number of exclusive subregions (basins), each of which corresponded to the imprint made by a single particle. This subdivision was made in such a way that the union of all subregions covered the region of interest of the image. To prevent basins from extending beyond the circular region of interest, this region was enclosed by a black background. In order to avoid oversegregation of the image, it was smoothed (Gaussian smoothing, $\sigma_x = \sigma_y = 10$) prior to the application of the watershed algorithm. The location, area, and integrated darkness of each subregion were determined using the same software. Utilizing a previously acquired calibration curve, the force F experienced by each particle was determined. Using the area A of the subregion, the equivalent stress S was calculated as $S = F/A$.

G. Statistical analysis

In order to reduce unwanted effects [44] of the averaging scheme used, the average force $\langle F \rangle$, stress $\langle S \rangle$, and area $\langle A \rangle$ were calculated for each experimental realization. Non-dimensional force, stress, and area variables were defined in terms of these averages as $f = F/\langle F \rangle$, $s = S/\langle S \rangle$, and $a = A/\langle A \rangle$. The results obtained for different realizations at a certain compression pressure were pooled, and the probability densities $\rho_f(f)$ and $\rho_s(s)$ were estimated by using the non-commercial statistical software R and its package LOCFIT [45,46,52]. Confidence intervals for $\rho_f(f)$ and $\rho_s(s)$ were obtained from the same software. The total force and stress averages, $\langle\langle F \rangle\rangle$ and $\langle\langle S \rangle\rangle$, respectively, were calculated as the averages of $\langle F \rangle$ and $\langle S \rangle$ over all experimental realizations at a certain compression pressure.

From the location of each imprint, the 2D pair-correlation function [6,47] $g(r)$ was estimated using the R package SPATSTAT and a translation edge correction. The 2D pair-correlation function may be defined as [6,47]

$$g(r) = \frac{1}{Nn_0\pi r} \sum_{i=1}^N \sum_{j=i+1}^N \delta(r_{ij} - r), \quad (1)$$

where N is the total number of marks, n_0 is the average density of marks, and r_{ij} is the distance between the centers of marks i and j . Calculations were performed for each experimental realization separately, and mean values and confidence intervals were determined from the results obtained for each compression pressure. Utilizing the same software, the mark-correlation function [47] $k_{mm}(r)$, where the mark $m = f$ or s , was estimated. Since the marks $m = f$ or s have been normalized, the mark-correlation function may be expressed as [6,47]

$$k_{mm}(r) = \frac{\sum_{i=1}^N \sum_{j=i+1}^N \delta(r_{ij} - r) m_i m_j}{\sum_{i=1}^N \sum_{j=i+1}^N \delta(r_{ij} - r)}. \quad (2)$$

Averages and confidence intervals were determined in the same way as for $g(r)$. Our $k_{ff}(r)$ corresponds to $K_1(r)$ of Ref. [6] and to $G(r)$ of Ref. [7].

III. RESULTS

A. Particle size and shape

The particle-size distribution was relatively narrow, with mean 0.92 mm and standard deviation 0.099 mm. Due to the presence of some dumbbell-shaped particles, the size distribution was positively skewed (skewness 0.72). Particles of this form may have resulted from incomplete separation or coalescence during spheronization. The distribution of aspect ratios was positively skewed (skewness 2.37), with mean 1.24 and standard deviation 0.22. With the exception of a small fraction of dumbbell-shaped particles, the main particle form was thus spherical, with some deviation from perfect sphericity.

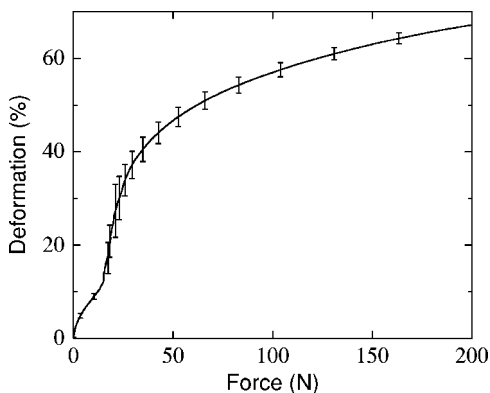


FIG. 1. Single-particle deformation in uniaxial compression. The error bars indicate standard deviations.

B. Compression of single particles

The single-particle deformation characteristics are shown in Fig. 1, which displays the single-particle deformation as a function of the applied force. As may clearly be seen in the figure, the slope of the force-deformation curve changes abruptly at a force around 15 N, which signifies a changed response of the particle to the applied force, due to failure of the particle attributed to plastic yield. It may also be seen that the standard deviation is particularly large in this region, because plastic yield starts at somewhat different forces for different particles. Following plastic deformation, the slope of the curve and the standard deviation gradually decrease. It is evident from the figure that a relatively small force causes considerable deformation of the particles.

In order to be able to use the carbon paper technique to measure forces experienced by single particles, we need to establish that a unique relationship exists between the force and some characteristic of the imprint made by the particle on the piece of white paper. As Fig. 2 shows, such a relationship exists between the force and the integrated darkness of the imprint. Although there is some random variation, there is a reasonable correlation between these two variables. It was found that forces ≥ 1 N could be detected with certainty.

C. Compression of particle packings

Having demonstrated the ability of the carbon paper technique to measure the forces of interest, we next consider compression of particle packings. Figure 3 shows representative background-corrected pictures of the imprints made by the particles on the piece of white paper placed on the lower punch. It may clearly be seen that the average intensity of the marks increases in proportion to the applied pressure. The pattern of imprints, moreover, appears more uniform for the higher compression pressures.

A similar trend was observed also for imprints on the piece of white paper placed on the upper punch (not shown). However, as a result of lateral particle motion during compression, the imprints tended to be more blurred. For this reason, we consider only the distributions of normal forces and stresses exerted on the lower punch in what follows.

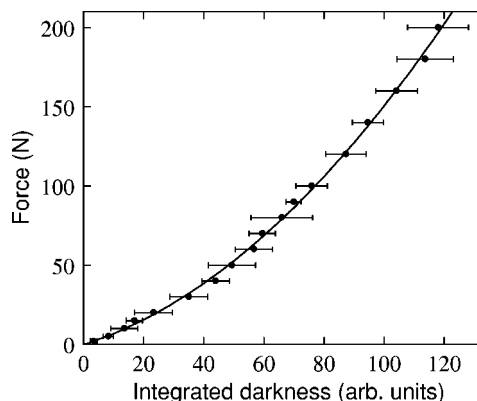


FIG. 2. Correlation between the force experienced by a single particle and the integrated darkness of its imprint. The solid line represents a polynomial fit to the data displayed in the figure. The error bars indicate standard deviations.

Let us now analyze the pictures of impressions, some of which are shown in Fig. 3, in more detail, starting with the total force and stress averages. As Fig. 4 shows, both $\langle\langle F \rangle\rangle$ and $\langle\langle S \rangle\rangle$ increase in direct proportion to the applied compression pressure. It may be seen that the data points corresponding to a compression pressure of 10 MPa lie somewhat above the lines through all other points. The most likely explanation for this deviation is that some particles at this applied pressure exerted a force below 1 N on the lower punch, which could not be detected because of limitations of the applied carbon paper technique. Since this deviation is rather small, the inability to detect small forces does not significantly affect the results. The linear relation between $\langle\langle F \rangle\rangle$ or $\langle\langle S \rangle\rangle$ and the applied compression pressure, moreover, indicates that the calibration used provided correct values of the force also for the largest forces, when significant particle deformation occurred.

It may also be seen that the average stress on the lower punch in all cases was approximately 60% of the applied compression pressure, i.e., the average stress exerted on the particles adjacent to the upper punch (neglecting the upper-

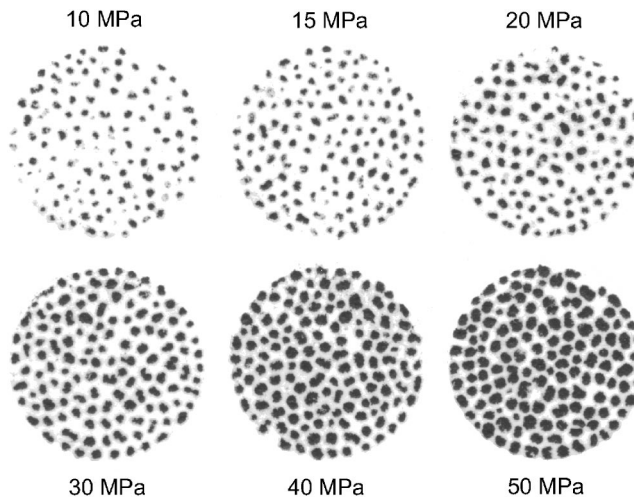


FIG. 3. Imprints made by particles on the piece of white paper placed on the lower punch at the compression pressures indicated.

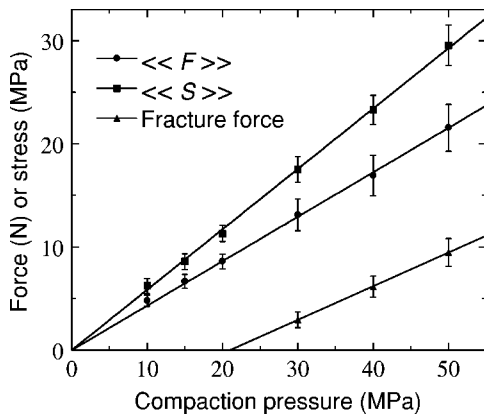


FIG. 4. Total averages for the force and stress experienced by single particles as a function of the compression pressure. Also shown is the force required to fracture compacts formed at pressures exceeding 30 MPa. The error bars indicate standard deviations.

punch-matrix friction force, which in all cases was ≤ 10 N). Thus 40% of the applied force was counteracted by die-wall friction, and this figure was independent of the magnitude of the applied pressure. This finding may be understood in terms of the classical Janssen effect [48]. Die-wall friction could have been reduced by using a lubricant, e.g., magnesium stearate. Since the presence of a lubricant may affect particle adhesion, and thus the strength of formed compacts, no lubricant was used in this study.

It was found that coherent compacts were formed at compression pressures ≥ 30 MPa. For forces exceeding 30 MPa, the fracture force (determined by diametrical compression according to the procedure described in Sec. II E) increased linearly with increasing pressure, as shown in Fig. 4. From the intersection of the linear fit with the abscissa it may be concluded that a pressure slightly larger than 20 MPa was required to form a coherent compact. This figure agrees well with observations made during the compression experiments: For 20 MPa some of the particles generally adhered to each other, but no compact was formed. No attempt was made to convert fracture forces to tensile strengths, because the compacts did not in general have the strength required to fail in tension [49].

Having discussed total averages and compact strengths, we next focus our attention on the distribution of normal forces and stresses. The probability density functions $\rho_f(f)$ and $\rho_s(s)$, estimated according to the procedure described in Sec. II G, are shown in Figs. 5(a) and 5(b). For clarity, all curves except the topmost ones have been translated downward.

The force distribution, shown in Fig. 5(a), exhibits the same general features for all compression pressures. It increases from a nonzero value at $f=0$ to a maximum at $f \approx 0.8$ and then shows an almost exponential decrease for larger values of f . The slope of the decay at large f is seen to increase with increasing compression pressure, but there is no clear indication of a crossover to a Gaussian behavior. The probability of finding small forces is seen to decrease considerably when the compression pressure is increased

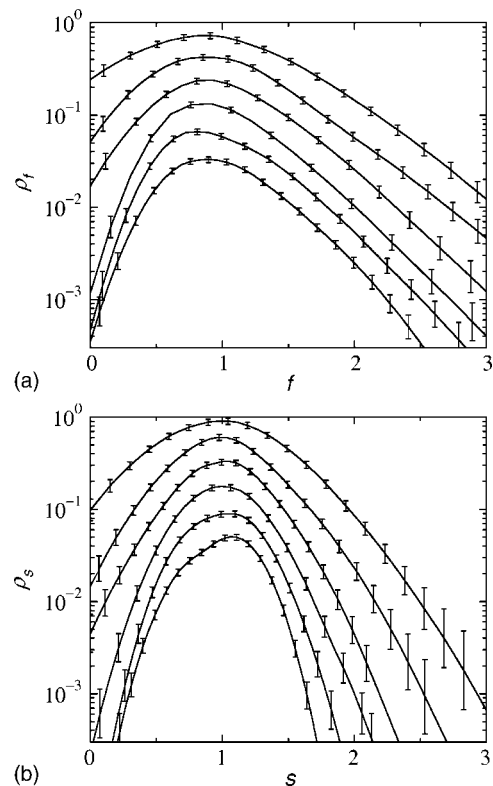


FIG. 5. Estimated density functions for the (a) force and (b) stress distributions. The curves display, from top to bottom, the results obtained at compression pressures of 10, 15, 20, 30, 40, and 50 MPa. The error bars indicate 95% confidence intervals. For clarity, all curves except the topmost ones have been translated downward.

from 10 to 30 MPa, but is virtually unchanged when the pressure is increased beyond 30 MPa.

The stress distribution, shown in Fig. 5(b), is considerably narrower than the force distribution, and is also more symmetric. The distribution is seen to exhibit a progressive narrowing with increasing compression pressure. It may also be seen that $\rho_s(s)$, when displayed on a linear-log scale as in Fig. 5, is parabolic in shape, indicating that the distribution of stresses is Gaussian (although it obviously has support for $s \geq 0$ only).

In order to better understand the relation between the force and stress distributions, we next investigate the correlation between the area corresponding to each particle and the force it experienced during compression. Motivated by the fact that the area for a perfectly Herzian contact scales as $f^{2/3}$ [50], we present our results on a log-log scale in Fig. 6 (note, however, that the area assigned to each particle is distinct from the area of the imprint). As may clearly be seen in the figure, a and f are positively correlated, and the overall trend is well represented by an expression of the form $a \propto f^\alpha$, as the solid regression lines show, but no unique relation exists between these two quantities. The regression lines are not intended as fits to the experimental data, but are included in the figure because they provide a *qualitative* explanation for the relation between the force and stress distributions (see below). Values of the exponent α , characterizing

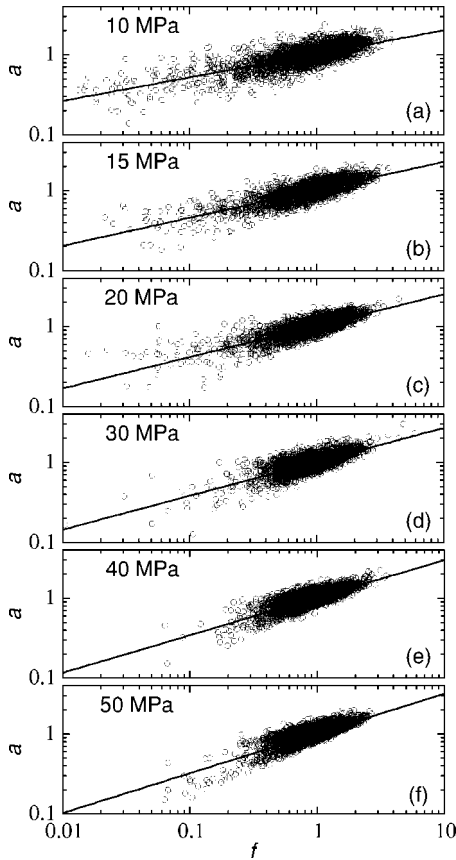


FIG. 6. Correlations between the nondimensional force f and area a at different compression pressures. Solid regression lines ($a \propto f^\alpha$) are drawn for all pressures.

the slope of the regression lines shown in Fig. 6, and the Pearson correlation coefficient R are given in Table I. Whereas the correlation coefficient R is more or less constant at approximately 0.8, the exponent α is seen to increase with increasing pressure, from approximately 0.3 to approximately 0.5. Hence, even though no unique relation exists between a and f , some of the features of the transition between $\rho_s(s)$ and $\rho_f(f)$ nevertheless appear to be possible to understand simply as resulting from a variable transformation of the form $s \propto f^{1-\alpha}$. For the highest pressures, when $\alpha \approx 0.5$, this simple relation would for instance transform an exponential decay of $\rho_f(f)$ for large forces to a Gaussian decay of $\rho_s(s)$ for large stresses.

TABLE I. Values of the exponent α at different compression pressures P obtained from the regression lines displayed in Fig. 6. The Pearson correlation coefficient R is also given.

P (MPa)	α	R
10	0.29	0.74
15	0.35	0.79
20	0.39	0.80
30	0.42	0.75
40	0.47	0.80
50	0.50	0.81

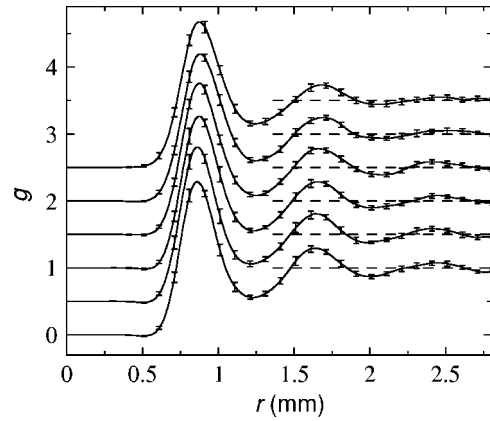


FIG. 7. Two-dimensional pair-correlation function. The curves display, from top to bottom, the results obtained at compression pressures of 10, 15, 20, 30, 40, and 50 MPa. The error bars indicate 95% confidence intervals. For clarity, all curves except the bottom one have been translated upward.

The spatial distribution of imprints may be described in terms of the 2D pair-correlation function $g(r)$. The pair-correlation function, estimated according to the procedure described in Sec. II G, is shown in Fig. 7. For clarity, all curves except the bottom one have been translated upward. The pair-correlation function exhibits for all compression pressures a shape that is typical of random packings of impenetrable particles. Since the particles cannot penetrate, $g(r)$ is virtually zero up to the smallest particle diameter. The pair-correlation function thereafter has a number of maxima, corresponding to the first, second, and higher-order coordination “shells.” There is, as expected, an evident short-range order, but no indication of a crystalline particle arrangement may be seen. From the location of the first maximum, the radius of the first coordination “shell” is seen to be ≈ 0.87 mm, and to decrease somewhat with increasing compression pressure. This value is slightly smaller than the mean projected-area diameter, which may indicate that the particles have been compressed laterally. However, since the particle-size distribution was positively skewed, the mean value overestimates the most probable particle diameter.

Having considered the spatial distribution of the imprints, we next investigate spatial force and stress correlations. The mark-distribution functions $k_{ff}(r)$ and $k_{ss}(r)$, estimated according to the procedure described in Sec. II G, are shown in Figs. 8(a) and 8(b), respectively. The upward-pointing triangles in Fig. 8 indicate the location of the first maximum of the pair-correlation function $g(r)$ at $r=r_{\max} \approx 0.87$ mm, while the downward-pointing ones show the location of the subsequent minimum of $g(r)$ at $r=r_{\min} \approx 1.24$ mm. As Fig. 8(a) shows, $k_{ff}(r)$ exhibits oscillations around the value unity, which is obtained in the absence of correlations. The amplitude of the oscillations is seen to decrease with increasing compression pressure and larger values of the interparticle distance r . It may also be seen that the location of the first maximum of $k_{ff}(r)$ almost coincides with the first minimum of $g(r)$, at least for compression pressures up to 30 MPa.

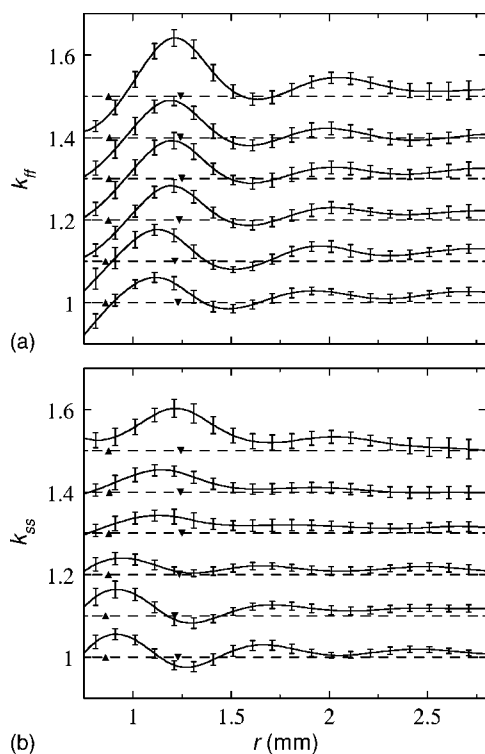


FIG. 8. Lateral (a) force and (b) stress pair correlations. The curves display, from top to bottom, the results obtained at compression pressures of 10, 15, 20, 30, 40, and 50 MPa. The error bars indicate 95% confidence intervals. For clarity, all curves except the bottom ones have been translated upward. The upward (downward) pointing triangles indicate the location of r_{\max} (r_{\min}), defined in the text.

As seen in Fig. 8(b), $k_{ss}(r)$ exhibits similar oscillations. For compression pressures < 30 MPa it is found that the location of the first maximum of $k_{ss}(r)$ almost coincides with the first minimum of $g(r)$, as for the force correlations. However, for pressures ≥ 30 MPa we instead find that the locations of both maxima almost coincide.

IV. DISCUSSION

With increasing compression pressure, the force distribution $\rho_f(f)$ changes in two ways: The probability of finding very small forces is greatly reduced and the slope of the exponential decay increases. No clear indication of a cross-over to a Gaussian behavior is found, however. These findings are consistent with the experimental results of Erikson *et al.* [9] and the simulations of Antony [33], but conflict with the observations made by Makse *et al.* [31]. According to our results, deformation has a less decisive effect on the force distribution than expected from the model of Ref. [32]. Assuming that the force-chain length decreases with increasing compression pressure, our results are also in qualitative agreement with the predictions of Ref. [37]. The observed changes in the wall-force distribution may be interpreted as resulting from an increased number of contacts [5], as would be expected for a compressed system [31], and therefore need not indicate that the bulk-force distribution changes.

We note that the shape of $\rho_f(f)$ for $f < 1$ is somewhat different from that obtained in Ref. [9], especially at compression pressures ≥ 30 MPa, for which a coherent compact was formed. Whereas Erikson *et al.* observed an exponential behavior of $\rho_f(f)$ for $f < 1$, our results are, for compression pressures ≥ 30 MPa, more consistent with a Gaussian behavior in this region. One consequence of this difference is that the peak height [defined as $\max \rho_f / \rho_f(0)$] is larger in our experiment (≈ 100 compared to $\lesssim 30$). Although an effect of the bottom layer of glass beads used in Ref. [9] cannot be ruled out, the most likely reason for this difference is that a coherent compact, capable of sustaining tensile stresses, is formed in our experiments.

It is interesting to note that the stress distribution $\rho_s(s)$ for all compression pressures investigated is considerably narrower than the force distribution and, furthermore, is consistent with a Gaussian behavior (but with support for $s \geq 0$ only). This finding may be interpreted as resulting from a positive correlation between the area corresponding to each particle and the force it experienced during compression. The positive correlation between force and area may also explain the behavior of the spatial force correlation function $k_{ff}(r)$: For the less probable interparticle distance $r = r_{\min}$, $k_{ff}(r)$ exhibits a distinctive positive correlation. This correlation may be an effect of a positive correlation between force and area.

At the most probable interparticle distance $r = r_{\max}$, $k_{ff}(r)$ may be seen to be slightly negative. Even though it is difficult to compare our results for disordered packings with those obtained using lattice models, we may note that negative lateral spatial force correlations have been predicted by the models of Refs. [32,37]. The negative correlation decreases somewhat with increasing compression pressure, and therefore agrees more with the simulation than the modeling results of Ref. [32]. The correlations, moreover, die off considerably faster than predicted in Ref. [37], probably as a result of the larger disorder present in our packings, in agreement with the result of other investigations [7,16]. An oscillatory behavior for $k_{ff}(r)$ has previously been observed for very small pressures [7]. However, these oscillations are in phase with those of $g(r)$, whereas the oscillations we observe essentially are out of phase.

The spatial stress correlation function $k_{ss}(r)$ exhibits an interesting evolution with increasing compression pressure. At $r = r_{\min}$, $k_{ss}(r)$ has a maximum for the lowest compression pressure, which gradually decreases in height and for pressures ≥ 30 MPa is replaced by a minimum. At this distance, the correlation thus changes from being positive to being negative. At the same time, the positive correlation at $r = r_{\max}$ becomes stronger. These observations show that the mode of stress transmission is different at low and high pressures, with the dividing line essentially corresponding to the formation of a compact. Before a compact has been formed, particles separated by unusually long distances from their neighbors appear to exert a larger than average stress on the confining surface, whereas these particles instead exert a smaller than average stress once a compact has been formed.

V. CONCLUSIONS

Utilizing the carbon paper technique and the watershed image-analysis algorithm it has been possible to determine not only the distribution of normal forces but also the distribution of corresponding normal stresses exerted by deformable particles on a confining wall. Whereas no indication of a crossover to a Gaussian decay at high forces was observed for the distribution of normal forces, the distribution of normal stresses was, for all compression pressures investigated, considerably more Gaussian in shape. This finding may be interpreted as resulting from a positive correlation between the area corresponding to each particle and the force it experienced during compression. More investigations are

necessary in order to fully understand this behavior. Spatial force and stress correlations were observed for distances smaller than three particle diameters, and the latter exhibited qualitatively different behaviors prior to and after the formation of a coherent compact, indicating that the mode of stress transmission changes when the compression pressure exceeds the minimum pressure required to form a coherent compact.

ACKNOWLEDGMENT

This study was part of a research program in Pharmaceutical Materials Science at Uppsala University.

-
- [1] H. M. Jaeger, S. R. Nagel, and R. P. Behringer, *Rev. Mod. Phys.* **68**, 1259 (1996).
- [2] P. G. de Gennes, *Rev. Mod. Phys.* **71**, S374 (1999).
- [3] C.-h. Liu, S. R. Nagel, D. A. Schecter, S. N. Coppersmith, S. Majumdar, O. Narayan, and T. A. Witten, *Science* **269**, 513 (1995).
- [4] J. H. Snoeijer, M. van Hecke, E. Somfai, and W. van Saarloos, *Phys. Rev. E* **67**, 030302(R) (2003).
- [5] J. H. Snoeijer, M. van Hecke, E. Somfai, and W. van Saarloos, *Phys. Rev. E* **70**, 011301 (2004).
- [6] D. M. Mueth, H. M. Jaeger, and S. R. Nagel, *Phys. Rev. E* **57**, 3164 (1998).
- [7] G. Løvoll, K. J. Måløy, and E. G. Flekkøy, *Phys. Rev. E* **60**, 5872 (1999).
- [8] D. L. Blair, N. W. Mueggenburg, A. H. Marshall, H. M. Jaeger, and S. R. Nagel, *Phys. Rev. E* **63**, 041304 (2001).
- [9] J. M. Erikson, N. W. Mueggenburg, H. M. Jaeger, and S. R. Nagel, *Phys. Rev. E* **66**, 040301(R) (2002).
- [10] V. Tournat, V. Zaitsev, V. Gusev, V. Nazarov, P. Béquin, and B. Castagnède, *Phys. Rev. Lett.* **92**, 085502 (2004).
- [11] F. Radjai, M. Jean, J. J. Moreau, and S. Roux, *Phys. Rev. Lett.* **77**, 274 (1996).
- [12] F. Radjai, S. Roux, and J. J. Moreau, *Chaos* **9**, 544 (1999).
- [13] C. Thornton, *Kona* **15**, 81 (1997).
- [14] C. Thornton and S. J. Antony, *Philos. Trans. R. Soc. London, Ser. A* **356**, 2763 (1998).
- [15] S. Luding, *Phys. Rev. E* **55**, 4720 (1997).
- [16] L. E. Silbert, G. S. Grest, and J. W. Landry, *Phys. Rev. E* **66**, 061303 (2002).
- [17] J. W. Landry, G. S. Grest, L. E. Silbert, and S. J. Plimpton, *Phys. Rev. E* **67**, 041303 (2003).
- [18] S. F. Edwards and R. B. S. Oakshott, *Physica D* **38**, 88 (1989).
- [19] P. Claudin and J.-P. Bouchaud, *Phys. Rev. Lett.* **78**, 231 (1997).
- [20] M. E. Cates, J. P. Wittmer, J.-P. Bouchaud, and P. Claudin, *Phys. Rev. Lett.* **81**, 1841 (1998).
- [21] A. J. Liu and S. R. Nagel, *Nature (London)* **396**, 21 (1998).
- [22] C. S. O'Hern, S. A. Langer, A. J. Liu, and S. R. Nagel, *Phys. Rev. Lett.* **86**, 111 (2001).
- [23] S. N. Coppersmith, C.-h. Liu, S. Majumdar, O. Narayan, and T. A. Witten, *Phys. Rev. E* **53**, 4673 (1996).
- [24] J. E. S. Socolar, *Phys. Rev. E* **57**, 3204 (1998).
- [25] J.-P. Bouchaud, M. E. Cates, and P. Claudin, *J. Phys. I* **5**, 639 (1995).
- [26] J. P. Wittmer, P. Claudin, M. E. Cates, and J.-P. Bouchaud, *Nature (London)* **382**, 336 (1996).
- [27] J. P. Wittmer, M. E. Cates, and P. Claudin, *J. Phys. I* **7**, 39 (1997).
- [28] P. Claudin, J.-P. Bouchaud, M. E. Cates, and J. P. Wittmer, *Phys. Rev. E* **57**, 4441 (1998).
- [29] S. F. Edwards and D. V. Grinev, *Granular Matter* **4**, 147 (2003).
- [30] D. Howell, R. P. Behringer, and C. Veje, *Phys. Rev. Lett.* **82**, 5241 (1999).
- [31] H. A. Makse, D. L. Johnson, and L. M. Schwartz, *Phys. Rev. Lett.* **84**, 4160 (2000).
- [32] M. L. Nguyen and S. N. Coppersmith, *Phys. Rev. E* **62**, 5248 (2000).
- [33] S. J. Antony, *Phys. Rev. E* **63**, 011302 (2001).
- [34] B. Müller, C. O'Hern, and R. P. Behringer, *Phys. Rev. Lett.* **77**, 3110 (1996).
- [35] J. H. Snoeijer and J. M. J. van Leeuwen, *Phys. Rev. E* **65**, 051306 (2002).
- [36] J. H. Snoeijer and J. M. J. van Leeuwen, *J. Stat. Phys.* **109**, 449 (2002).
- [37] M. Nicodemi, *Phys. Rev. Lett.* **80**, 1340 (1998).
- [38] G. Alderborn and M. Wikberg, in *Pharmaceutical Powder Compaction Technology*, edited by G. Alderborn and C. Nyström (Marcel Dekker, New York, 1996), Chap. 12.
- [39] C. Nyström and P.-G. Karehill, in *Pharmaceutical Powder Compaction Technology* (Ref. [38]) Chap. 2.
- [40] C. Askling, L. Wagberg, and M. Rigdahl, *J. Mater. Sci.* **33**, 1997 (1998).
- [41] L. Vincent and P. Soille, *IEEE Trans. Pattern Anal. Mach. Intell.* **13**, 583 (1991).
- [42] J. B. T. M. Roerdink and A. Meijster, *Fund. Inform.* **41**, 187 (2001).
- [43] Å. Tunón, E. Börjesson, G. Frenning, and G. Alderborn, *Eur. J. Pharm. Sci.* **20**, 469 (2003).
- [44] C. S. O'Hern, S. A. Langer, A. J. Liu, and S. R. Nagel, *Phys. Rev. Lett.* **88**, 075507 (2002).
- [45] C. R. Loader, *Ann. Stat.* **24**, 1602 (1996).

- [46] C. Loader, *Local Regression and Likelihood* (Springer, New York, 1999).
- [47] D. Stoyan and H. Stoyan, *Fractals, Random Shapes and Point Fields: Methods of Geometrical Statistics*, Wiley Series in Probability and Mathematical Statistics (Wiley, Chichester, 1994).
- [48] H. A. Janssen, *Z. Ver. Dt. Ing.* **39**, 1045 (1895).
- [49] J. T. Fell and J. M. Newton, *J. Pharm. Sci.* **59**, 688 (1970).
- [50] K. L. Johnson, *Contact Mechanics* (Cambridge University Press, Cambridge, U.K., 1985).
- [51] Available at <http://rsb.info.nih.gov/ij/>
- [52] Both available at <http://www.r-project.org/>